CHAPTER III

A POSSIBLE FAR-INFRARED QUANTUM CASCADE LASER

In this chapter we describe in detail the possible far-infrared quantum-cascade-laser design with conduction-band potential illustrated in Figure 1.1. In particular, we introduce a possible chemical composition and discuss the resulting tunneling potential as a function of the voltage drop V applied across the central tunneling region. We furthermore determine the voltage-drop dependence of the quasi-bound resonant levels and find that the so-called quantum-confined Stark effect[1] at $V_{sym} \approx 23$ mV causes an avoided crossing, corresponding to the minimal value, $D \geq D(V_{sym}) = 10.9$ meV, of the subband separation. By design, this voltage drop V_{sym} is contained within the range, 12 mV $\lesssim V \lesssim$ 30 mV of voltage drops that ensures both a strong current injection exclusively into the upper subband and a fast lower-level escape rate whose voltage-drop dependence we estimate.

We also consider the quantum-confined Stark effect on the quasi-bound wavefunction symmetry.[1,2] Specifically we demonstrate that the special applied bias V_{sym} causing the avoided crossing at the same time also restores a near-exact *wavefunction*-inversion symmetry in the still asymmetric potential. Moreover, we introduce the center-of-charge separation (dipole matrix element) as a simple measurement of the wavefunction symmetry (overlap.) Finally we discuss the voltage-drop dependence of the wavefunction-inversion symmetry which we in Chapter IV find significantly affects the intersubband electron-electron scattering rates.

We furthermore describe the experimental determination[3] of the intersubband decay rate in the corresponding *isolated* asymmetric quantum-well structure.[3,4] This structure is formed by the same double-quantum-well potential which constitutes the core of the Figure 1.1 tunneling structure but surrounded instead by very thick (modulation-doped) $Al_{0.3}Ga_{0.7}As$ barriers. The experimental observation[3] of a very small intersubband decay rate, $1/\tau \lesssim 0.03$ meV at $T \lesssim 50$ K, observed at weak optical pumping of this quantum-well structure motivated our choice of the specific tunneling structure with potential shown in Figure 1.1.

The main focus of this dissertation is an estimate of the intersubband decay and resulting population inversion arising with a strong current injection into the Figure 1.1 tunneling structure. In this chapter we argue that the total *single*-particle decay, Γ_{sp}, of the nonequilibrium current-injected upper-subband occupation remains approximately bounded by the experimental value, $1/\tau \approx 0.03$ meV (at $T \lesssim 50$ K) observed at a weak optical pumping.[3] At the same time we emphasize that no such experimental bound applies to the *nonequilibrium* electron-electron intersubband scattering. This observation motivates our subsequent detailed study of the nonequilibrium electron-electron scattering reported in Chapter IV.

III.A Schematics of far-infrared quantum-cascade-laser design

Figure 3.1 shows schematics of the asymmetric double-quantum-well tunneling structure for which we in this dissertation estimate the intersubband decay and resulting population inversion. Specifically, the *top* panel of Figure 3.1 shows a possible chemical composition with a central tunneling region (of extension $L_{QB} =$ 243 Å) surrounded by n-doped digital Al Ga$_a$Aslloy leads. The tunneling region is formed as a double-quantum-well structure surrounded by two $L_B = 30$ Å $Al_{0.3}Ga_{0.7}As$ tunneling barriers allowing final tunneling rates into and out from the lowest two quasi-bound resonant levels, E_1 and E_2.

The *bottom* panel of Figure 3.1 shows a schematics of the corresponding tunneling potential in equilibrium and in the absence of any electron charging effects.* The solid bars indicates the equilibrium positions of the quasi-bound resonant levels E_1^0 and E_2^0. Table 3.1 list the physical parameters characterizing this equilibrium potential with all energy positions listed relative to the equilibrium potential in the GaAs wells.

The choice of a digital $Al_xGa_{1-x}As$ alloy with an $x \approx 0.05$ Aluminum content raises both the emitter and collector band edge, $\phi_L^0 = \phi_R^0 = 36$ meV, relative to the GaAs quantum-well potential. The equilibrium positions of the emitter and collector chemical potentials, $\mu_{L/R}^0 = \phi_{L/R}^0 + 10$ meV, is given by the assumed $N_{3D} \sim 10^{17}$ cm^{-3} lead doping concentration. We assume that this doping concentration ensures a fixed thickness, $\mu_L - \phi_L = \mu_R - \phi_R = 10$ meV, of the emitter and collector Fermi sea also out of equilibrium. The raised positions of the emitter

* We shall neglect such self-consistent charging effects on the potential and level positions throughout the entire dissertation.

FIGURE 3.1 Schematics of hypothetical far-infrared quantum-cascade-laser design in equilibrium (schematics of tunneling potential at a finite voltage drop illustrated in Figure 1.1.) The *top* panel shows (a possible) chemical composition of the asymmetric double-quantum-well tunneling structure. In particular, the structure comprises the central tunneling region of total extension $L_{QB} = 243$ Å surrounded n-doped leads formed as digital $\mathrm{Al}_x\mathrm{Ga}_{1-x}\mathrm{As}$ alloys. The *bottom* panel shows a schematics of the resulting tunneling potential in equilibrium (and neglecting all electron-charging effects.) Table 3.1 list the physical parameters characterizing this tunneling potential and the equilibrium positions, E_1^0 and E_2^0, of the quasi-bound resonant levels (indicated by the solid bars. For the emitter ('L') and collector ('R') leads we assume a value $x \approx 0.05$ for the Al-content in the digital $\mathrm{Al}_x\mathrm{Ga}_{1-x}\mathrm{As}$ alloys. As illustrated, this choice raises the equilibrium positions of the lower emitter and collector band edge, $\phi_L^0 = \phi_R^0 = 36$ meV, relative to the bottom of the GaAs quantum wells. An assumed $N_{3D} \sim 10^{17}$ cm^{-3} lead doping concentration positions the emitter and collector chemical potentials at $\mu_{L/R}^0 = \phi_{L/R}^0 + 10$ meV. We shall assume that the relation $\mu_L - \phi_L = \mu_R - \phi_R = 10$ meV also holds true in the presence of a finite voltage-drop V applied across the central tunneling region.

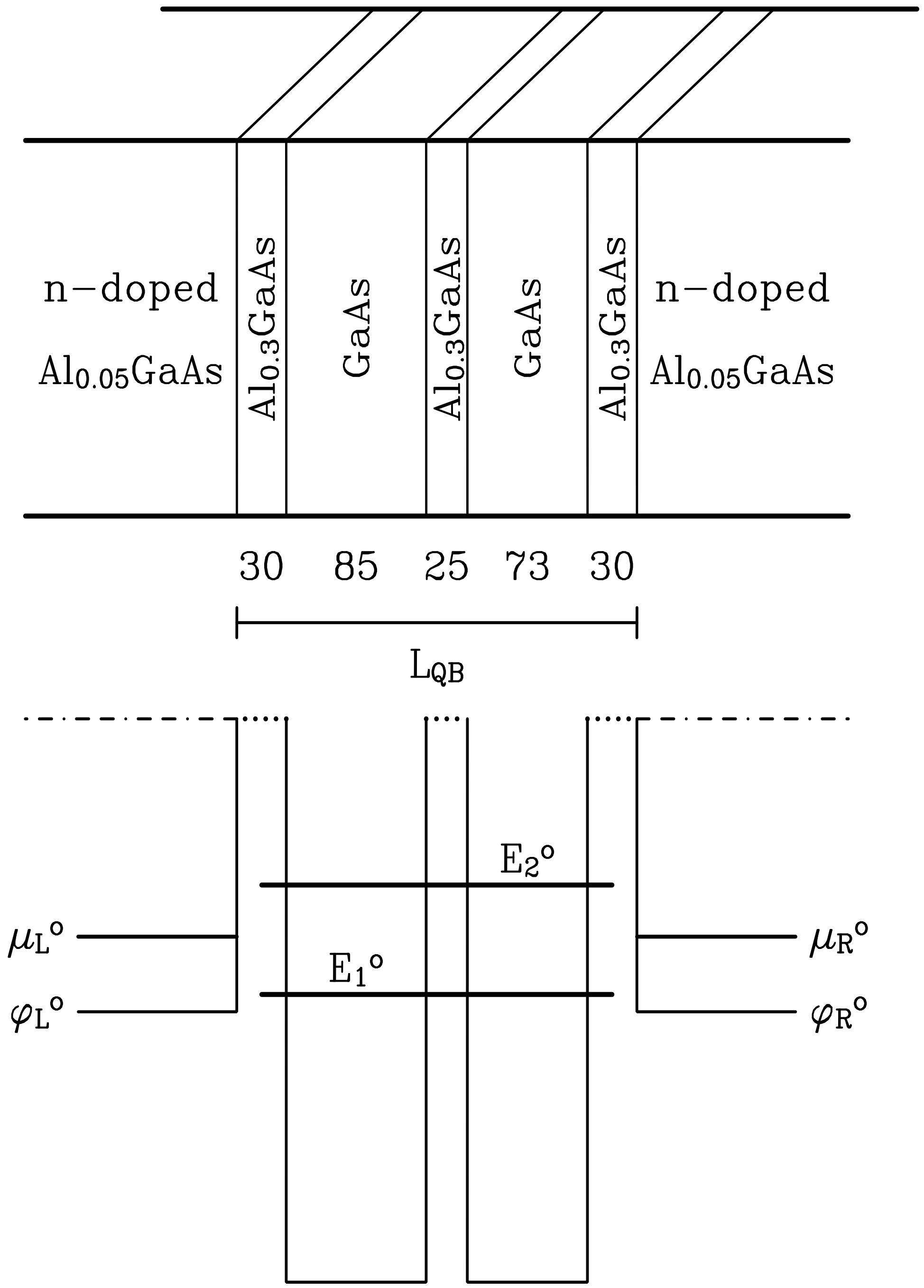

n−doped
$Al_{0.05}GaAs$
$Al_{0.3}GaAs$
GaAs
$Al_{0.3}GaAs$
GaAs
$Al_{0.3}GaAs$
n−doped
$Al_{0.05}GaAs$
30
85
25
73
30
L_{QB}
$E_2°$
$\mu_L°$
$\mu_R°$
$E_1°$
$\varphi_L°$
$\varphi_R°$

FIGURE 3.1

TABLE 3.1 Parameters characterizing the equilibrium tunneling potential, electron occupation, and position of quasi-bound resonant levels, E_1^0 and E_2^0, for specific tunneling structure with schematics shown in Figure 3.1. We neglect all electron charging effects and list the equilibrium tunneling-barrier heights ($\phi_B^0 = 214$ meV) and resonant-level energy positions (E_1^0 and E_2^0) relative to the equilibrium position of the GaAs quantum wells. The choice of digital $Al_xGa_{1-x}As$ ($x \approx 0.05$) leads raises the equilibrium positions of the emitter and collector lower band edges, $\phi_L^0 = \phi_R^0 = 36$ meV. The equilibrium positions, $\mu_{L/R}^0 - \phi_{L/R}^0 = 10$ meV, of the emitter and collector chemical potentials, μ_L and μ_R, are given by the assumed lead doping concentration $N_{3D} \sim 10^{17}$ cm^{-3}. We emphasize that the raised positions of the emitter and collector band edges allow both a strong upper-subband current injection and a fast lower escape rate at just a moderate voltage drop, 12 mV $\lesssim V \lesssim$ 30 mV, see Table 3.2.

TABLE 3.1

Physical quantity	Symbol	Equilibrium value
Total central region thickness	L_{QB}	243 Å
Barrier thickness	L_B	30 Å
$Al_{0.3}Ga_{0.7}As$-barrier potential	ϕ_B^0	214 meV
Emitter/collector band edge	$\phi_{L/R}$	36 meV
Lead doping concentration	N_{3D}	$\sim 10^{17}\text{cm}^{-3}$
Equilibrium chemical potential	$\mu_L^0 = \mu_R^0$	46 meV
Thickness of Fermi sea	$\mu_{L/R}^0 - \phi_{L/R}^0$	10 meV
Upper resonant level	E_2^0	52.9 meV
Lower resonant level	E_1^0	38.3 meV
Subband separation	$\Delta^0 \equiv E_2^0 - E_1^0$	14.6 meV

and collector band edges implies in particular that only a moderate voltage drop V applied across the tunneling region results in an exclusive upper-subband current injection. Assuming also that the tunneling escape rate out to the collector can maintain a finite population inversion in spite of the intersubband decay, a net stimulated emission will then obtain at a frequency ω_Δ given by the far-infrared subband separation $\Delta \equiv E_2 - E_1 \approx 11$ meV.

III.B The nonequilibrium current flow and optical response

In this section we describe for the Figure 3.1 tunneling structure both the nonequilibrium current flow and the regimes of the optical response. Specifically we estimate (a) the quantum-confined Stark effect[1] on (i.e., the voltage-drop dependence of) the quasi-bound resonant levels, (b) the range of voltage drops that results in the so-called emission regime with both an exclusive upper-subband current injection (Γ_e) and a fast lower-level escape rate (Γ_{c1},) and finally (c) the voltage-dependence of the tunneling escape rates, Γ_{c1} and Γ_{c2}, within this emission regime. Table 3.2 summarizes these estimates.

We shall as previously stated neglect all electron charging effects and thus assume, in the presence of a finite voltage drop V, a constant internal field $F_{dc} = V/L_{QB}$ within the tunneling region. We assume in particular a simple variation of the emitter and collector lower band edges and chemical potentials,

$$\phi_{L(R)} = \phi_0 + (-)eV/2, \tag{1}$$

$$\mu_{L(R)} = \mu_0 + (-)eV/2, \tag{2}$$

relative to equilibrium values, $\phi_{L(R)} = \phi_0$, and $\mu_{L(R)} = \mu_0$.

TABLE 3.2 Voltage-drop dependence of tunneling potential, the escape rates (Γ_{c1}, Γ_{c2} and Γ_{e},) and of the quasi-bound resonant-level wavefunctions, $\Psi_1(x)$ and $\Psi_2(x)$, for the tunneling potential schematically illustrated in Figure 3.1. We neglect electron-charging effects, that is, the self-consistent effects on the potential arising with a finite electron occupation. We assume in particular a constant internal field $F_{dc} = V/L_{QB}$ within the tunneling region (as illustrated in Figure 1.1) in the presence of a finite voltage drop V which raises/lowers the emitter/collector band edges, $\phi_{L/R} = \phi^0_{L/R} + / - eV/2$, and chemical potentials, $\mu_{L/R} = \phi_{L/R} + 10$ meV. We also neglect electron charging effects in estimating the voltage-drop dependence of the quasi-bound resonant levels (described further in Figure 3.3.) The so-called emission regime with both an exclusive upper-subband current injection (Γ_e) *and* a fast lower-subband tunneling escape (Γ_{c1}) requires both of the following conditions: $\mu_L > E_2 > \phi_L$ and $\phi_L > E_1 > \mu_R$. As indicated this regime with possible net stimulated intersubband emission results at voltage-drops 12 mV $\lesssim V \lesssim$ 30 mV. Within the limited range of voltage drops we find only a moderate variation of the current injection rate of the tunneling escape rates Γ_{c1} and Γ_{c2}, see text. The table furthermore indicates the voltage drop dependence of the optical (dipole) transitions matrix element and center-of-charge separation, discussed further in Figs. 3.2 and 3.3. For completeness the table also list the assumed operating temperature, $T \leq 25$ K and $T \ll (\mu_L - E_2)$. The first of these criteria ensures a vanishing value of the total *single*-electron decay, $\Gamma_{se} \leq 0.03$ meV, see text. The second conditions for the temperature, $T \ll (\mu_L - E_2)$, arises because we in Chapter IV evaluate the nonequilibrium electron-electron scattering at zero temperature only.

TABLE 3.2

Physical quantity	Symbol	Value in equilibrium	At finite applied bias V
Emitter/collector chemical potential	$\mu_{L/R}$	$\mu^0_{L/R} = 46$ meV	$\mu_{L/R} = \mu^0_{L/R} + / - eV/2$
Emitter/collector band edge	$\phi_{L/R}$	$\phi^0_{L/R} = 36$ meV	$\phi_{L/R} = \phi^0_{L/R} + / - eV/2$
Upper resonant level	E_2	$E^0_2 = 52.9$ meV	$E_2(V) \geq 50.8$ meV†
Lower resonant level	E_1	$E^0_1 = 38.3$ meV	$E_1(V) \leq 39.8$ meV†
Subband separation	$\Delta \equiv E_2 - E_1$	$\Delta^0 = 14.6$ meV	$\Delta(V) \geq 10.9$ meV†
Emission regime	—	—	12 meV $\lesssim eV \lesssim 30$ meV
Lower-level escape rate	Γ_{c1}	—	0.4 meV $\lesssim \Gamma_{c1} \lesssim 0.6$ meV
Upper-level escape rate	Γ_{c2}	—	0.9 meV $\lesssim \Gamma_{c2} \lesssim 1.1$ meV
Emitter injection rate	Γ_e	—	$\Gamma_e \sim \Gamma_{c2}/2$
Optical transition matrix element	$\langle \Psi_2 \vert x \vert \Psi_1 \rangle$	38.8 Å	$\langle \Psi_2 \vert x \vert \Psi_1 \rangle (V) \leq 51.2$ Å‡
Center-of-charge separation§	$\langle \Psi_2 \vert x \vert \Psi_2 \rangle$	67.2 Å	$\vert \langle \Psi_2 \vert x \vert \Psi_2 \rangle \vert \geq 0^\ddagger$
Assumed temperature	T	$T \leq 25$ K	and $T \ll \mu_L - E_2(V)$

† See Figure 3.3 $\quad$ ‡ See Figure 3.5 $\quad$ § Measured from $\langle \Psi_1 | x | \Psi_1 \rangle \equiv 0$

We estimate the resonant-level positions E_1 and E_2 (and corresponding quasi-bound wavefunctions $\Psi_1(x)$ and $\Psi_2(x)$) as given by the lowest two bound energy levels[5] of the corresponding isolated double-quantum-well structure (investigated in Ref. 3,4) when subjected to the same internal field, $F_{dc} = V/L_{QB}$. Within this approximation we proceed to determine the quantum-confined Stark effect,[1] that is, the voltage drop-dependence of the (quasi-bound) levels.

The *top* panel of Figure 3.2 shows schematics of tunneling potential, resonant level positions E_1^0 and E_2^0 (solid bars,) and corresponding wavefunctions $\Psi_1^0(x)$ and $\Psi_2^0(x)$ in equilibrium. Both the upper- and lower-level wavefunction extend throughout both quantum wells but more of the upper- (lower)-level wavefunction is concentrated in sleightly narrower right (wider left) quantum well. There is thus in equilibrium a finite center-of-charge separation, $\langle\Psi_2^0|x|\Psi_2^0\rangle - \langle\Psi_1^0|x|\Psi_1^0\rangle \approx 67$ Å.

Applying a finite voltage drop raises (lowers) the (bottom of) the left (right) quantum well relative to the quantum-well center and will eventually force the lower (upper) quasi-bound level into the narrower right (wider left) quantum well. This quantum-confined stark effect[1] must in particular cause an avoided crossing of the (quasi-bound) level position at some intermediate voltage drop $V = V_{sym}$ with a minimal subband separation $\Delta^s = \Delta(V_{sym}) = 22.9$ meV.

The *bottom* panel of Figure 3.2 shows the tunneling potential, energy levels (solid bars,) and wavefunctions $\Psi_{1,2}^s(x)$ at this avoided crossing V_{sym}. The set of dashed bars indicate the corresponding equilibrium positions of the resonant level positions and we observe that the quantum-confined Stark effect does result in a finite voltage-drop variation of the quasi-bound energy positions E_1 and E_2.

FIGURE 3.2 Quantum-confined Stark effect[1] on the quasi-bound resonant levels and on the corresponding wavefunction-inversion symmetry.[2] *Top* panel shows the position of the (quasi-bound) resonant levels $E^0_{1,2}$ (solid bars) and corresponding approximate wavefunctions $\Psi^0_{1,2}(x)$ in equilibrium. Note that more of the upper- (lower-)level wavefunction is situated in the narrower rightmost (wider leftmost) quantum well and the equilibrium wavefunctions are characterized by a finite center-of-charge separation, $\langle\Psi^0_2|x|\Psi^0_2\rangle - \langle\Psi^0_1|x|\Psi^0_1\rangle > 0$. Applying a finite voltage drop V thus initially lowers (raises) the upper (lower) resonant levels until, eventually (at $V > V_{sym}$) the center of charge is reversed and more of the upper- (lower-)level wavefunction is concentrated in the wider, but leftmost (narrower, but rightmost,) quantum well. At a finite voltage drop, $V = V_{sym} = 22.9$ meV, this so-called quantum-confined Stark effect[1] results in an avoided crossing of the level positions with a minimal subband separation, $\Delta^s = \Delta(V_{sym}) = 10.9$ meV. The *bottom* panel illustrates the tunneling potential, resonant level positions, E_1 and E_2, and corresponding wavefunctions, $\Psi^s_{1,2}(x)$, at this avoided crossing, $V = V_{sym}$. For comparison the bottom panel also shows the equilibrium positions of the resonant levels (dashed bars.)

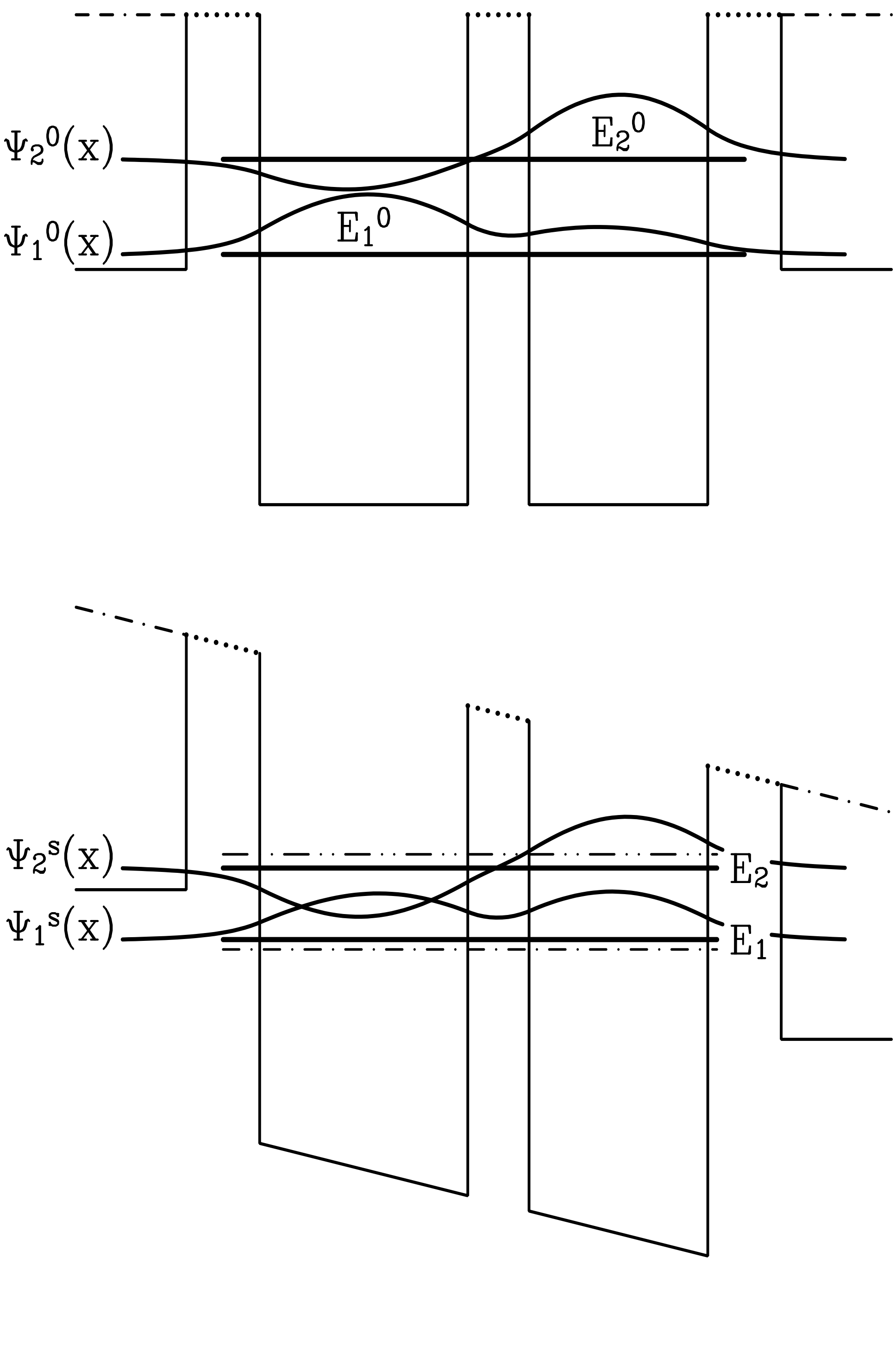

FIGURE 3.2

FIGURE 3.3 Avoided crossing of resonant-level positions *and* regimes of the nonequilibrium current flow and optical response. *Top* panel determines the quantum-confined Stark effect[1] on the resonant levels and determines the minimum subband separation arising at the avoided crossing between $E_1(V)$ and $E_2(V)$. *Bottom* panel identifies the qualitative regimes of the far-infrared optical response of the tunneling structure based on the estimate level positions $E_{1,2}(V)$. Specifically, at voltage drop $V \lesssim$ 10 mV, the upper- (lower-)resonant level is still located above (within) the emitter (collector) Fermi sea, $E_2 > \mu_L$ ($\mu_R > E_1$) and there is no an upper-subband current injection but a finite lower-subband occupation density. Radiation tuned to the subband separation thus results in a (resonantly enhanced) absorption. *However,* as indicated by the pair of downwards arrows, only a slightly increased voltage drop, 12 mV $\lesssim V \lesssim$ 30 mV, ensures both $\mu_L > E_2 > \phi_L$ *and* $\phi_L > E_1 > \mu_R$. Such moderate voltage drops thus provides an exclusive upper-subband current injection (Γ_e) — since E_2 but not E_1 is located within the emitter Fermi sea — and a fast lower-subband tunneling escape rate (Γ_{c1}) — because the lower level is situated above the collector Fermi surface and all final collector states are available for the tunneling-out process. Under these conditions the lower level is only populated by intersubband scattering and the current injection may thus provide a finite intersubband population inversion and a net stimulated emission as indicated by the pair of downward arrows.

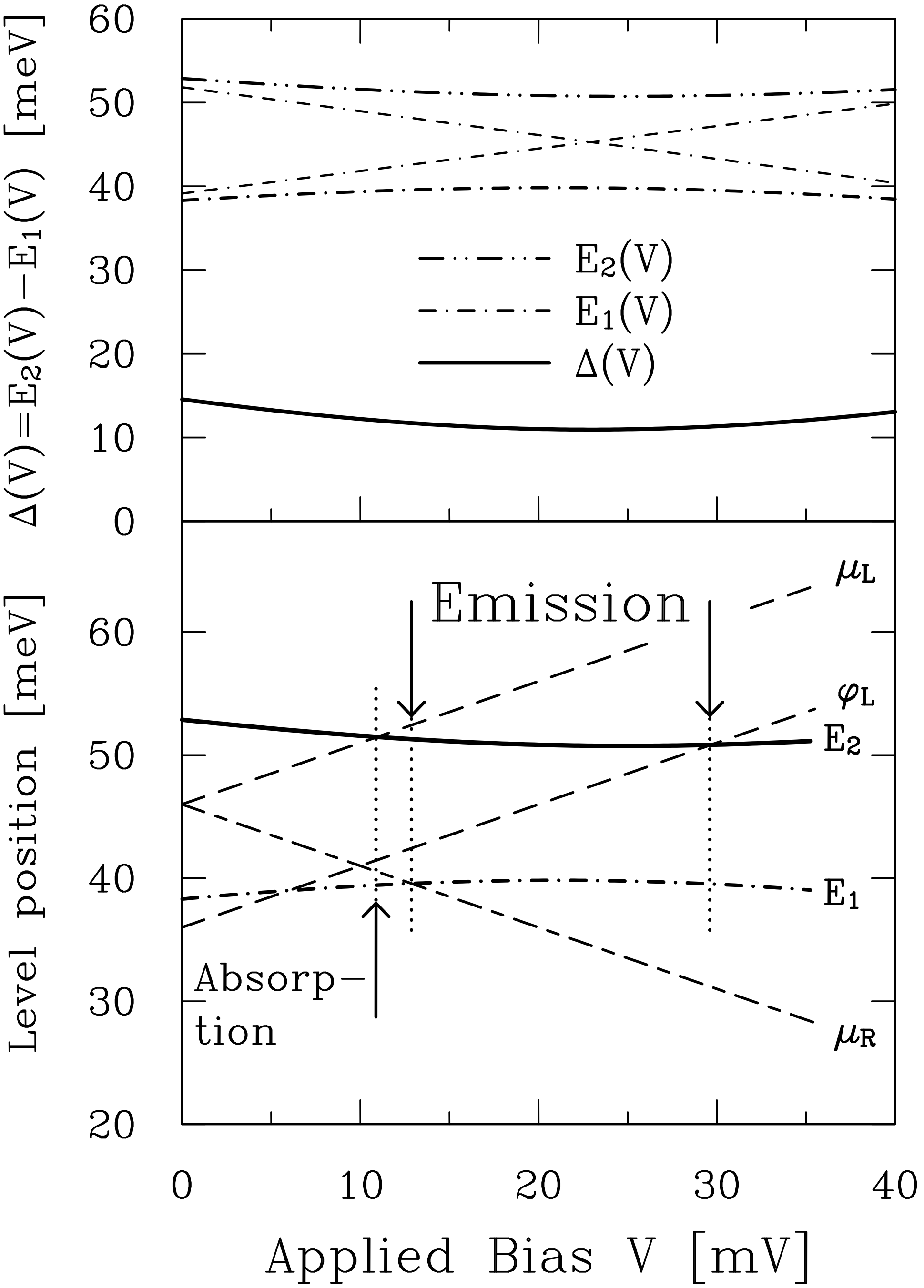

60
50
40
30
20
10
0
$\Delta(V)=E_2(V)-E_1(V)$ [meV]
$E_2(V)$
$E_1(V)$
$\Delta(V)$
Level position [meV]
Emission
μ_L
φ_L
E_2
E_1
μ_R
Absorp-
tion
0
10
20
30
40
Applied Bias V [mV]

FIGURE 3.3

Top panel of Figure 3.3 shows the voltage-drop variation of the level positions and also illustrates the avoided crossing. The panel also shows the variation of the subband separation, $\Delta(V) \equiv E_2 - E_1 > \Delta^s$.

The *bottom* panel of Figure 3.3 identifies the regimes of the nonequilibrium optical response in the tunneling structure. Specifically, the lower panel of Figure 3.3 compares the estimated variation of the resonant level positions with the assumed voltage-drop dependence of the emitter lower band edge, ϕ_L, and with the emitter and collector chemical potential, μ_L and μ_R (see Eqs. (1) and (2).) The knowledge of the relative positions of E_1 and E_2 *and* of ϕ_L, μ_L, and μ_R allows a determination of the (nonequilibrium) optical regimes.

Consider first the situation at a small applied voltage drop, $V \lessapprox 10$ mV. The upper level E_2 then remains located above the emitter chemical potential and there is only a vanishing upper-subband electron occupation. The lower level is on the other hand situated *below* the collector chemical potential and there will be a finite lower-subband occupation density. As a consequence, radiation with a frequency tuned to the subband separation will thus experience a resonantly enhanced intersubband absorption, as indicated by the upward arrow in the bottom panel of Figure 3.3.

However, as indicated by the pair of downward arrows in Figure 3.3, it takes only a moderate voltage drop

$$12 \text{ mV} \lessapprox V \lessapprox 30 \text{ mV}, \tag{3}$$

to ensure both of the following conditions for a possible net intersubband stimulated emission

$$\phi_L \leq E_2 \leq \mu_L, \tag{4}$$

$$\phi_L > E_1 > \mu_R. \tag{5}$$

As a result of the condition Eq. (4) there will be a finite current injection Γ_e directly into the upper subband. In contrast, because the lower level E_1 is situated below ϕ_L, there will be no current injection directly into the lower subband. Moreover, because Eqs. (4) and (5) ensures $E_2, E_1 > \mu_R$, there will be fast tunneling escape rates, Γ_{c2} and Γ_{c1}, out from both resonant levels (as none of the finite collector states are thus occupied.)

Adapting the discussion in Section I.B we may estimate the tunneling escape rates as follows

$$\Gamma_{cj=1,2} = \frac{v_j}{2L_{QB}} T_R(E_j) \equiv \frac{\sqrt{2E_r/m_e^*}}{2L_{QB}} T_R(E_j). \tag{6}$$

Here $v_j = \sqrt{2E_j/m_e^*}$ denotes the velocity of resonant level $E_{j=1,2}$ and

$$T_R(E_j) \approx 16\Theta(E_j - \phi_R) \frac{\sqrt{E_j(E_j - \phi_R)}}{\phi_B - E_j} \exp(-2L_B\sqrt{2m_e^*(\phi_B - E_j)}), \tag{7}$$

denotes the probability for tunneling through the $L_B = 30$ Å thick barriers for which we assume a constant potential height $\phi_B = 214$ meV.

As listed in Table 3.2, within the range, Eq. (3), of voltage drops allowing the potential realization of a net stimulated emission, we predict from Eqs. (6) and (7) only a moderate voltage-drop dependence of the escape rates

$$0.40 \text{ meV} \lesssim \Gamma_{c1} \lesssim 0.56 \text{ meV}, \tag{8}$$

$$0.93 \text{ meV} \lesssim \Gamma_{c2} \lesssim 1.09 \text{ meV}. \tag{9}$$

Such a moderate variation with the voltage drop (as well as the possible electron-charging effects on these tunneling rates) can (if desired) be negated by a small charge in the width of the tunneling barriers L_B which dramatically modifies the tunneling probability, see Eq. (7).

III.C The wavefunction-symmetry variation

Figure 3.2 above also illustrate the significant quantum-confined Stark effect[1] on the symmetry of the quasi-bound levels.[2] In particular, it is clear from the *bottom* panel of Figure 3.2 that the voltage drop restores an approximate *wavefunction*-inversion symmetry at the avoided crossing, $V = V_{sym}$. In this section we (a) demonstrate this inversion-symmetry is almost exact, (b) introduce the center-of-charge separation $\langle\Psi_2|x|\Psi_2\rangle - \langle\Psi_1|x|\Psi_1\rangle$ (dipole matrix element $\langle\Psi_2|x|\Psi_1\rangle$) as a qualitative measure of the wavefunction asymmetry (overlap,) and (c) determine the wavefunction symmetry and overlap as function of the voltage drop V.

The vanishing center-of-charge separation,

$$\langle\Psi_2^s|x|\Psi_2^s\rangle - \langle\Psi_1^s|x|\Psi_1^s\rangle \equiv 0, \tag{10}$$

characterizing the avoided crossing at V_{sym} automatically ensures an approximate inversion symmetry of the corresponding wavefunctions. However, for the Figure 3.1 tunneling structure we find an almost exact symmetry because there is only a small difference in the widths of the individual quantum wells.

Figure 3.4 verifies that the wavefunction-inversion symmetry is almost exact at the avoided crossing, $V = V_{sym}$. Specifically, the top and bottom panels of Figure 3.4 test the expected anti-symmetry and symmetry,

$$-\Psi_2^s(x_0 - x) = \Psi_2^s(x - x_0), \tag{11}$$

$$\Psi_1^s(x_0 - x) = \Psi_1^s(x - x_0), \tag{12}$$

FIGURE 3.4 Test of the restored near-exact *wavefunction*-inversion symmetry at avoided crossing, $V = V_{sym} = 22.9$ mV. The set of vertical dashed lines indicates the positions of both the central quantum-well barrier and of the external tunneling barriers confining the wavefunctions, $\Psi^s_{1,2}(x)$. The quantum-confined Stark effect[1] causes at $V = V_{sym}$ an avoided crossing in the resonant level positions, see Figure 3.3. By symmetry the center-of-charge separation must vanish at this avoided crossing, $\langle\Psi^s_2|x|\Psi^s_2\rangle - \langle\Psi^s_1|x|\Psi^s_1\rangle \equiv 0$, (see also Figure 3.5) and the quantum-confined Stark effect must thus in addition restore an approximate inversion-symmetry of the corresponding wavefunctions,[2] $\Psi^s_{1,2}(x)$. For the specific far-infrared tunneling structure (with schematics shown in Figure 3.1) this *wavefunction*-inversion symmetry is very accurate. Specifically, the top panel demonstrates that the upper-resonant-level wavefunction which vanishes at $x = x_0$ (indicated by vertical dotted line) is almost completely *anti-symmetric,* $\Psi^s_2(x - x_0) = -\Psi^s_2(x_0 - x)$. The *bottom* panel correspondingly demonstrates that the lower-resonant-level wavefunction is *symmetric,* $\Psi^s_1(x - x_0) = \Psi^s_1(x_0 - x)$, also around $x = x_0$.

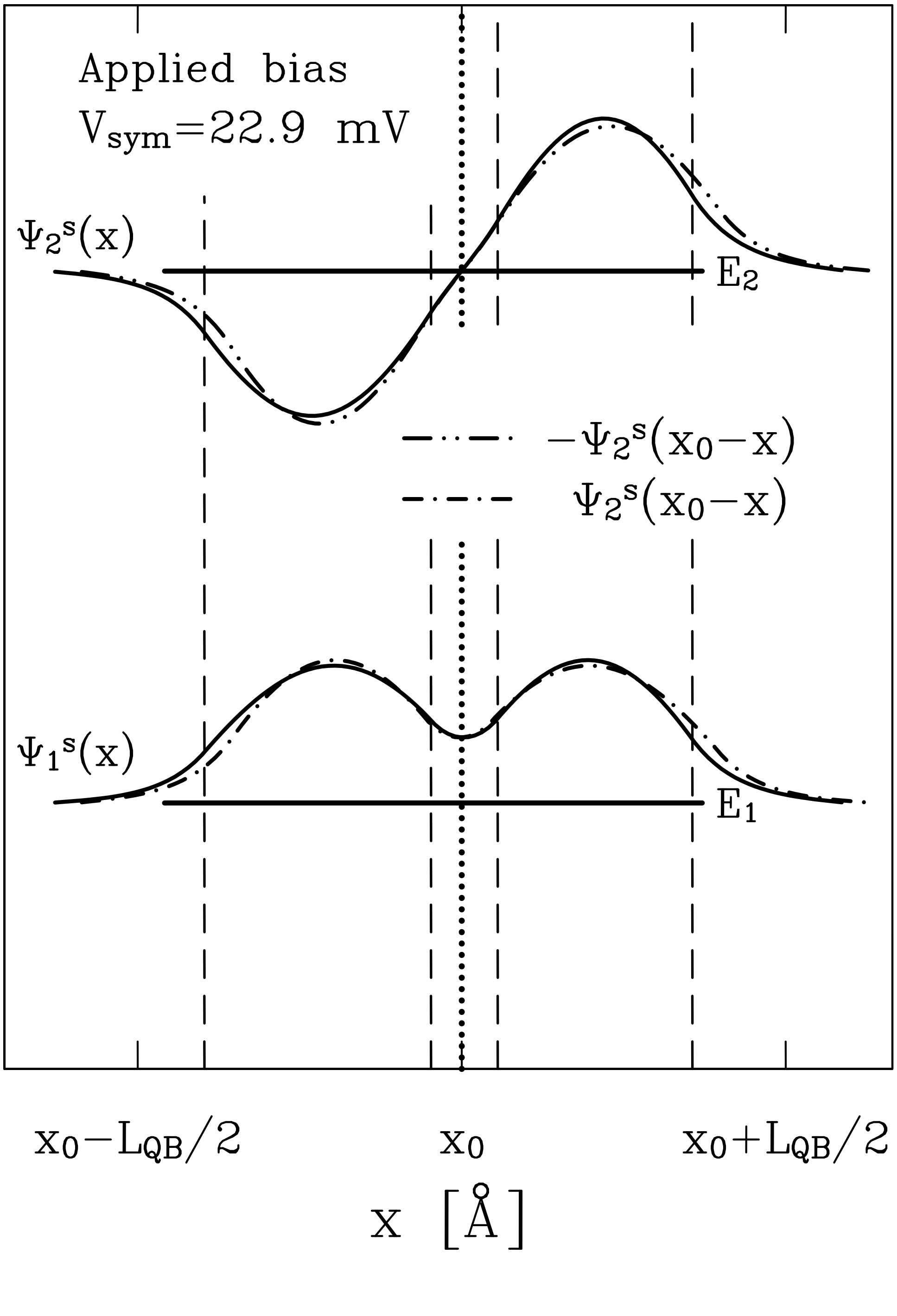

Applied bias
V_{sym}=22.9 mV
$\Psi_2{}^s(x)$
E_2
$-\Psi_2{}^s(x_0-x)$
$\Psi_2{}^s(x_0-x)$
$\Psi_1{}^s(x)$
E_1
$x_0-L_{QB}/2$
x_0
$x_0+L_{QB}/2$
x [Å]

FIGURE 3.4

of upper- and lower-level wavefunction $\Psi_2^s(x)$ and $\Psi_1^s(x)$ assuming the node x_0 of $\Psi_2^s(x)$ forms the inversion point. The excellent agreement between the left- and right-hand-side expressions of Eqs. (11) and (12) verifies the near-exact *wavefunction*-inversion symmetry restored at V_{sym} in the still asymmetric potential (see bottom panel of Figure 3.2.)

This near-exact correspondence between the vanishing center-of-charge separation, Eq. (10), and a restored inversion symmetry, Eqs. (11) and (12), suggest $\langle\Psi_2|x|\Psi_2\rangle - \langle\Psi_1|x|\Psi_1\rangle$ as a qualitative measure of the wavefunction *asymmetry* at $V \neq V_{sym}$. We also introduce the dipole matrix element $\langle\Psi_2|x|\Psi_1\rangle$ as a qualitative measure of the wavefunction overlap.

To motivate these qualitative measures of the wavefunction characteristics we consider a simple two-level model and assume we can expand the upper- and lower-level wavefunctions at voltage drop V,

$$\Psi_2^{(V)}(x) = \cos(\chi(V - V_{sym}))\,\Psi_2^s(x) - \sin(\chi(V - V_{sym}))\,\Psi_1^s(x), \tag{13}$$

$$\Psi_1^{(V)}(x) = \sin(\chi(V - V_{sym}))\,\Psi_2^s(x) + \cos(\chi(V - V_{sym}))\,\Psi_1^s(x), \tag{14}$$

exclusively in terms of $\Psi_{1,2}^s(x)$. We furthermore assume these $V = V_{sym}$ wavefunctions has an exact inversion symmetry

$$\langle\Psi_2^s|x|\Psi_2^s\rangle \equiv \langle\Psi_1^s|x|\Psi_1^s\rangle \equiv x_0, \tag{15}$$

around the node x_0 of $\Psi_2^s(x)$.

At $V = V_{sym}$ we assume the unitary angle χ in Eqs. (13) and (14) take the value, $\chi(V = V_{sym}) \equiv 0$. To determine the voltage drop dependence of the unitary angle in general $\chi(V - V_{sym})$, we expand the Hamiltonian H_V for the electron motion in the confinement potential into H_s (corresponding to $V = V_{sym}$) and a correction term H_1,

$$H_V = H_s + H_1, \tag{16}$$

$$H_1 = -e(V - V_{sym})\frac{(x - x_0)}{L_{QB}}. \tag{17}$$

At a general value of χ the Hamiltonian H_V has the off-diagonal matrix elements

$$\langle\Psi_2^{(V)}|H_V|\Psi_1^{(V)}\rangle = \langle\Psi_2^{(V)}|H_s|\Psi_1^{(V)}\rangle + \langle\Psi_2^{(V)}|H_1|\Psi_1^{(V)}\rangle, \tag{18}$$

$$\langle\Psi_2^{(V)}|H_s|\Psi_1^{(V)}\rangle = \frac{\Delta^s}{2}\sin(2\chi(V - V_{sym})), \tag{19}$$

$$\langle\Psi_2^{(V)}|H_1|\Psi_1^{(V)}\rangle = -\frac{e(V - V_{sym})}{L_{QB}}\cos(2\chi(V - V_{sym}))\langle\Psi_2^s|x|\Psi_1^s\rangle, \tag{20}$$

where Δ^s denotes the subband separation at $V = V_{sym}$. The combined off-diagonal matrix element, Eq. (18), must vanish for the correct value of $\chi(V - V_{sym})$. Hence we obtain the condition

$$\tan(2\chi(V - V_{sym})) = \frac{\langle\Psi_2^s|x|\Psi_1^s\rangle}{L_{QB}}\frac{2e}{\Delta^s}(V - V_{sym}). \tag{21}$$

We note that in the limit $V \to \pm\infty$ we obtain the value $\chi(V \to \pm\infty) \equiv \pm\pi/4$ and that in particular the $V \to \infty$ limit results in upper- and lower-level wavefunctions

$$\Psi_2^{(\infty)}(x) = \Psi_L(x) \equiv \left[\Psi_2^s(x) - \Psi_1^s(x)\right]/\sqrt{2}, \tag{22}$$

$$\Psi_1^{(\infty)}(x) = \Psi_R(x) \equiv \left[\Psi_2^s(x) + \Psi_1^s(x)\right]/\sqrt{2}, \tag{23}$$

concentrated (although not completely localized) in the right and left quantum well, respectively. Within our two-level description these wavefunctions represent the largest possible wavefunction asymmetry and the variation $-\pi/4 < \chi(V - V_{sym}) < \pi/4$ of the unitary angle present itself as a qualitative measure of this asymmetry.

FIGURE 3.5 Voltage-drop variation of the center-of-charge separation, $\langle\Psi_2|x|\Psi_2\rangle - \langle\Psi_1|x|\Psi_1\rangle$ and of the dipole-matrix element $\langle\Psi_2|x|\Psi_1\rangle$ (top panel) around avoided crossing, $V = V_{sym}$, identified in bottom panel. Solid curve in *top* panel shows dramatic variation around $V = V_{sym}$ of the center-of-charge separation introduced (see text) as a simple measure of the wavefunction symmetry. In Chapter IV we demonstrate this symmetry-variation causes a dramatic voltage-drop variation of the nonequilibrium electron-electron scattering rate $\Gamma_{22\to21}$ (involving two upper-subband electrons of which only one decays to subband E_1.) The double-dashed-dotted curve in top panel shows a moderate voltage-drop variation (also related to the wavefunction symmetry, see text) of the dipole-matrix element — a simple measure of the wavefunction overlap. In Chapter IV we find this moderate variation of $\langle\Psi_2|x|\Psi_1\rangle$ causes a significant variation also of the nonequilibrium electron-electron scattering rate $\Gamma \equiv \Gamma_{22\to11}$ (involving two upper-subband electrons which both decay two subband E_1.) We emphasize that the avoided crossing, $V = V_{sym}$, results (by design) within the range of voltage drops — identified in the lower panel — which ensures an exclusive upper-subband current injection. We have arranged this so that our predictions for a dramatic symmetry/voltage-drop dependence of the nonequilibrium electron-electron scattering rate is relevant for the range of possible current injections. This choice does not, however, ensures the maximum possible intersubband population inversion as explained in Chapter IV.

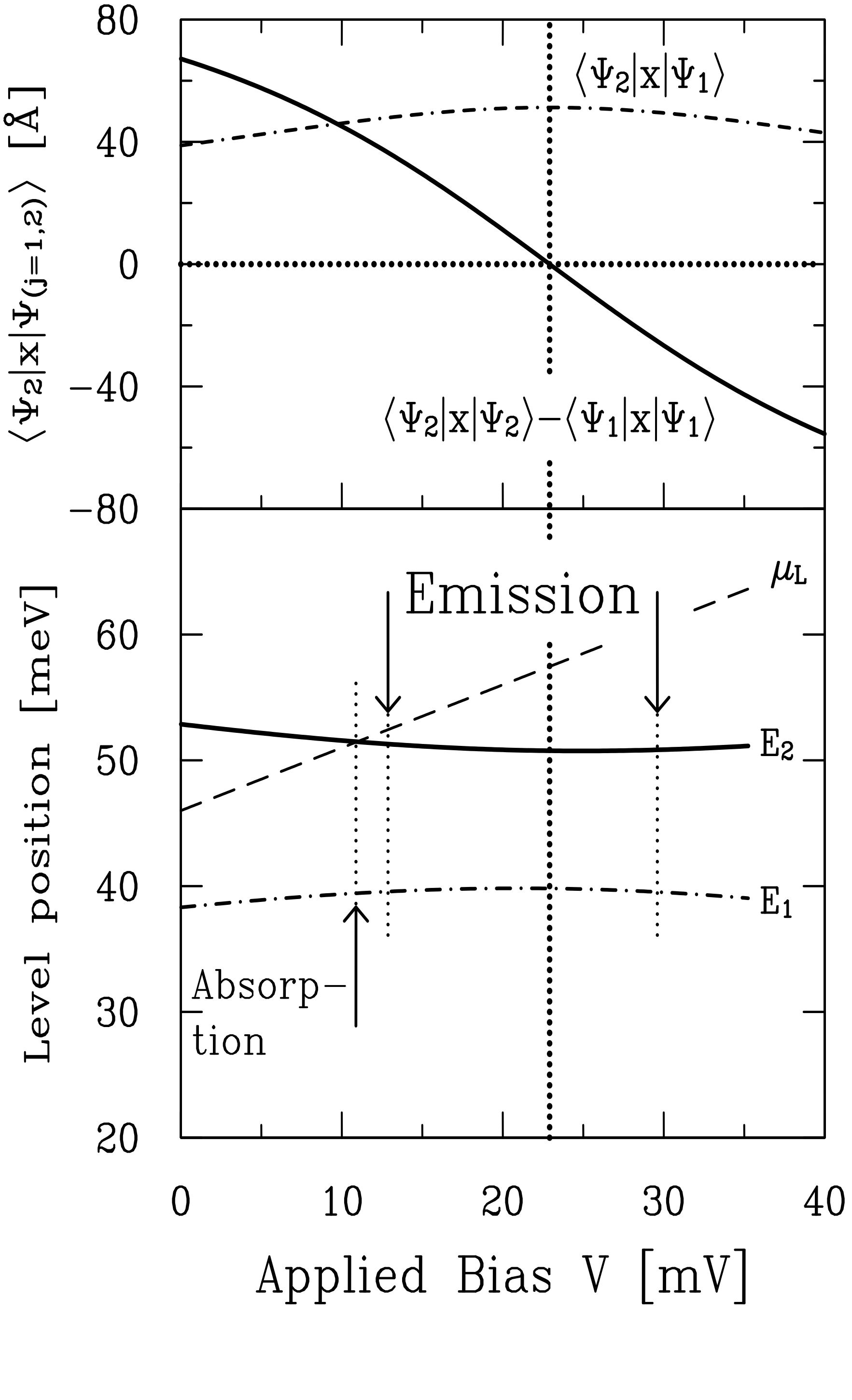

80
40
0
−40
−80
$\langle\Psi_2|x|\Psi_{(j=1,2)}\rangle$ [Å]
$\langle\Psi_2|x|\Psi_1\rangle$
$\langle\Psi_2|x|\Psi_2\rangle-\langle\Psi_1|x|\Psi_1\rangle$
Emission
μ_L
E_2
E_1
Absorp-
tion
60
50
40
30
20
Level position [meV]
0
10
20
30
40
Applied Bias V [mV]

FIGURE 3.5

Moreover, the variation of this unitary angle $\chi(V - V_{sym})$ is directly reflected in the center-of-charge separation

$$\langle \Psi_2^{(V)} | x | \Psi_2^{(V)} \rangle - \langle \Psi_1^{(V)} | x | \Psi_1^{(V)} \rangle = -2 \sin(2\chi(V - V_{sym})) \langle \Psi_2^s | x | \Psi_1^s \rangle, \tag{24}$$

and in the dipole matrix element

$$\langle \Psi_2^{(V)} | x | \Psi_1^{(V)} \rangle = \cos(2\chi(V - V_{sym})) \langle \Psi_2^s | x | \Psi_1^s \rangle. \tag{25}$$

We shall assume these relations also holds approximately for the actual potential problem for which the eigenvalues and wavefunctions must of course be determined not through Eq. (21) but using a Schrödinger-solver code.[5] This assumption finally motivates the introduction of the center-of-charge separation, $\langle \Psi_2 | x | \Psi_2 \rangle - \langle \Psi_1 | x | \Psi_1 \rangle$, as a qualitative measure of the wavefunction asymmetry.

To motivate our use of the dipole matrix element, $\langle \Psi_2 | x | \Psi_1 \rangle$, as a qualitative measure of the wavefunction overlab we mention that Eq. (24) is consistent with an expected maximum (minimal) overlap at $V = V_{sym}$ ($V \to \pm\infty$.)

The top panel of Figure 3.5 shows the calculated voltage-drop dependence of both the dipole matrix element, solid curve, and the center-of-charge separation, dashed curve. The center-of-charge separation (measure of wavefunction asymmetry) exhibits a significant voltage-drop dependence. The charge-separation vanishes at $V = V_{sym}$ but the magnitude quickly rises and begins to saturate (essentially at the inter-quantum-well separation ~ 90 Å) at $|V - V_{sym}| \gtrsim V_{sym}$.* The observed strong quantum-confined Stark effect on the wavefunction asymmetry causes a dramatic variation on the nonequilibrium electron-electron scattering, see Chapter IV.

* The beginning saturation at $V = 0$ is also evident in the top panel of Figure 3.2 where the upper- (lower)-level charge-density is found concentrated mostly in the narrower right (wider left) quantum-well.

Finally we observe that there is in contrast only a moderate variation of the dipole matrix element (measure of the wavefunction overlap,) although this variation is of course still given by the wavefunction asymmetry, see Eq. (24). The largest value obtains at the avoided crossing, $V = V_{sym}$, but the dipole matrix element (and hence the optical transition rate) remains significant within the entire (potential) emission regime identified in the bottom panel.

III.D Experimental determination of intersubband decay

Our choice of the specific tunneling structure shown in Figure 3.1 is motivated by the observed[3] small intersubband decay rate, $1/\tau \lesssim 0.03$ meV arising at temperatures $T \lesssim 50$ K under weak optical pumping of the corresponding isolated quantum-well structure.[3,4] We shall argue in Section III.E below that the value $1/\tau = 0.03$ meV constitute a strict experimental bound on the impurity, interface-defect and on the acoustic-phonon scattering. Since we furthermore find that the thermally activated phonon emission can be ignored at temperatures $T \leq 25$ K we feel justified in assuming that $\Gamma_{sp} = 0.03$ meV constitutes at $T \leq 25$ K an experimental bound on the total *single*-electron decay (Γ_{se}) arising with the nonequilibrium current injection.

The experimental determination of the intersubband decay rate by Dr. J. Heyman *et al.*, at the Free Electron Laser lab at U. C. Santa Barbara used a photo-voltage measurement to determine the net optical excitation. By furthermore balancing the net intersubband absorption with the intersubband decay they obtained an estimate for the net decay.

The investigated structure[3,4] comprises the same central asymmetric double-quantum-well structure as in our Figure 3.1 tunneling structure but surrounded instead by two 5200 Å digital $Al_{0.3}Ga_{0.7}As$-alloy barrier layers. A pair of delta-doped Si layers more than 700 Å away provides a finite quantum-well sheet density $N_s \sim 10^{11}$ cm^{-2} without introducing a large ionized-impurity scattering within the double-quantum-well potential. An ohmic contact is formed to this sheet-density of quantum-well electrons which together with a top gate evaporated onto the heterostructure surface $d \approx 5000$ Å above the double-quantum-well potential forms a dielectric capacitor.

The experimental measurements are undertaken in the presence of a finite bias, V_G = -0.8 V, applied between the top gate and the quantum-well electrons. This result[6] in an estimated sheet-density of $N_s = 1.18 \times 10^{11}$ cm^{-2} sufficient to ensure a strong optical response (absorption.) The capacitance charge, eN_s, remains essentially constant during the short (~ 1 μs) pulses of the optical pumping with the Free Electron Laser radiation.

The dashed curve in the *bottom* panel of Figure 3.6 shows the equilibrium chemical potential* μ_0 as a function of the temperature T. The equilibrium distribution is at low temperature, $T \ll 25$ K, characterized as a lower-subband Fermi sea, i.e., with a near-constant chemical potential (Fermi surface) and with the sheet-density $N_s = 1.18 \times 10^{11}$ cm^{-2} located almost exclusively in the lower subband. However, at temperatures $T \gtrsim 25$ K there is a dramatic drop in the chemical potential μ_0 and the system can at $T \gtrsim 50$ K essentially be described by a Boltzmann distribution. There is in particular a finite upper-subband occupation which within this

* We shall in the following discussion of the optical pumping experiment define the energy zero-point by $E_1 \equiv 0$.

FIGURE 3.6 Comparison of measured net intersubband decay rate $1/\tau$ (triangles) and theory estimate of optical-phonon induced decay rates $\Gamma_{LO}^{op}/\Gamma_{LO}^{ci}$ (top panel) for the optical-pumped/current-injected distribution described by chemical potential μ_0/μ_2 (given in bottom panel.) At temperatures $T \lesssim 25$ K, our theory estimate Γ_{LO}^{op} is in reasonable agreement with the measured intersubband decay rates which can be described[3] by thermal activation energy $\Omega_{LO} - \Delta \approx 24$ meV. The measured value, $1/\tau = 0.03$ meV constitute a strict bound on the total impurity, interface-defect, and acoustic-phonon scattering also in the presence of a strong upper-subband current injection. Our theory estimate, Γ_{LO}^{ci}, of the corresponding optical-phonon induced decay is evaluated for the maximum possible upper-subband current injection below $\mu_L \equiv \mu_2 + E_2$. This rate Γ_{LO}^{ci} does exceed the decay rate Γ_{LO}^{op} for the weakly optically pumped distribution. However, even with the current-injected distribution the optical-phonon induced decay rate Γ_{LO}^{ci} is still thermally activated and can essentially be ignored at temperatures $T \leq 25$ K. We feel, as a consequence, ourselves justified in assuming that also the total *single*-electron decay rate, Γ_{se}, at $T \leq 25$ K remains bounded by the experimental value $1/\tau = 0.03$ meV.

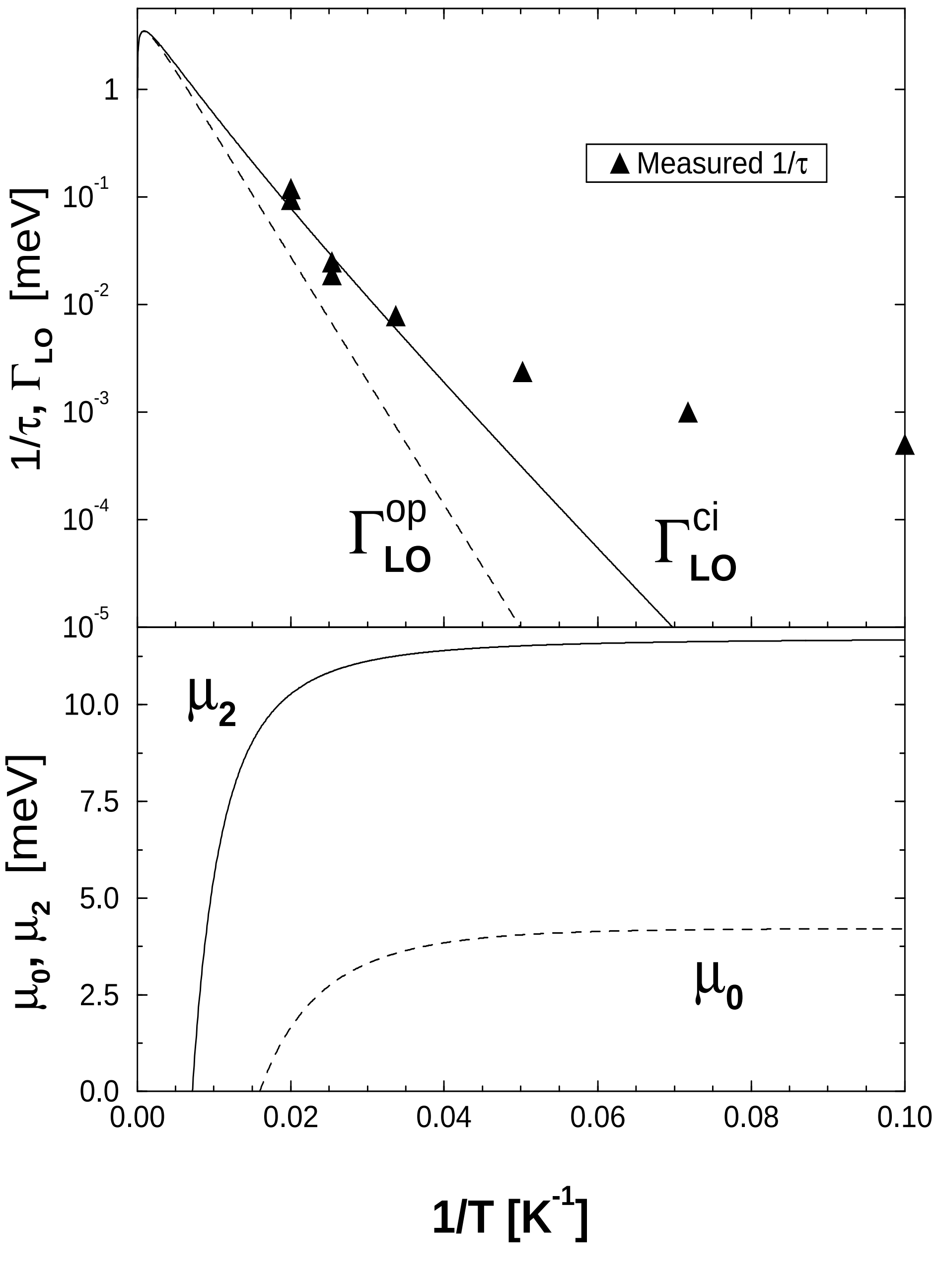

1
10^{-1}
10^{-2}
10^{-3}
10^{-4}
10^{-5}
$1/\tau$, Γ_{LO} [meV]
▲ Measured $1/\tau$
Γ_{LO}^{op}
Γ_{LO}^{ci}
10.0
7.5
5.0
2.5
0.0
μ_0, μ_2 [meV]
μ_2
μ_0
0.00
0.02
0.04
0.06
0.08
0.10
$1/T$ [K^{-1}]

FIGURE 3.6

Boltzmann description is estimated at

$$\left.\frac{n_2^0}{N_s}\right|_B = \frac{\exp(-\Delta/T)}{1+\exp(-\Delta/T)} \approx 0.07 N_s \qquad \text{at } T = 50 \text{ K}, \tag{26}$$

while the actual (Fermi-Dirac) distribution yields $n_2^0(50\text{ K}) \approx 0.1 N_s$.

Under such equilibrium conditions, i.e., in the absence of any optical pumping we gave of course a balance between the intersubband transitions,

$$\frac{n_2^0}{\tau_{2\to1}^0} \equiv \frac{n_1^0}{\tau_{1\to2}^0}, \tag{27}$$

where $1/\tau_{2\to1}^0$ $(1/\tau_{1\to2}^0)$ denotes the transition rate from subband E_2 (E_1) to E_1 (E_2) — averaged over the equilibrium electron-distribution.

The optical pumping by the Free Electron Laser radiation excites an intersubband plasmon and increases the upper-subband occupation to n_2. At strong optical pumping intensities and/or with very slow plasmon relaxation by intra- and intersubband scattering it may be necessary[7] to include coherent effects in a discussion of the correspondingly increased resulting intersubband decay. However, we believe that it is appropriate to neglect such coherent effects at weak optical pumping and at $T \sim 50$ K where the approximate Boltzmann electron distribution ensures[8] a fast (pico-second) electron-electron scattering and in particular plasmon decay, see for example Ref. 9. We assume one may also neglect plasmon effects at the intermediate temperatures, $25 \text{ K} \lesssim T \lesssim 50$ K and shall describe the effects of the weak optical pumping simply in terms of a change in the upper-subband single-particle distribution function.

Specifically, with a weak optical excitation $\delta n_2 \equiv n_2 - n_2^0$ we expect a linear increase (decrease) of the intersubband scattering from subband E_2 (E_1) to E_1

$(E_2,)$ resulting in a *net* decay:

$$\frac{\delta n_2}{\tau} = \delta n_2 \left(\frac{1}{\tau_{2\to 1}} + \frac{1}{\tau_{1\to 2}} \right). \tag{28}$$

Moreover, we assume that the transition rates $1/\tau_{2\to 1}$ and $1/\tau_{1\to 2}$ in Eq. (28) obtains as a simple averaging over the weakly optically excited distribution and shall neglect the change $1/\tau_{1\to 2}$ with optical pumping. On the other hand, in the resulting approximation,

$$\frac{1}{\tau} \approx \frac{1}{\tau_{2\to 1}} + \frac{n_2^0}{n_1^0} \frac{1}{\tau_{2\to 1}^0}. \tag{29}$$

for the net intersubband decay we note that the optically excited rate, $1/\tau_{2\to 1}$, exceeds the equilibrium rate $1/\tau_{2\to 1}^0$ because the optically excited distribution results in a stronger optical-phonon emission.*

The increased (net) intersubband decay, $\delta n_2/\tau$, must be balanced by the net absorption. Assuming a pump frequency ω (tuned to the intersubband optical transitions) and intensity $S_{FEL}(\omega)$ we have,

$$\frac{\delta n_2}{\tau} \equiv \frac{S_{FEL}(\omega)}{\omega} \sigma_{ab}(\omega)(n_2 - n_1), \tag{30}$$

where we have introduced the lower-subband occupation density $n_1 = N_s - n_2$, and the absorption cross section $\sigma_{ab}(\omega)$.

The key idea in the experimental determination involves using an estimate for the center-of-charge separation to determine the total number $\delta n_2 \equiv (n_2 - n_2^0)$ of optically excited electrons from a measurement of the photovoltage. To make this connection we reiterate that the top contact and the N_s quantum-well electrons

* The thermal activation energy for optical-phonon emission in the equilibrium distribution is given by the phonon frequency, Ω_{LO}, itself. However, the thermal activation energy in the (weakly) optically excited distribution is reduced to $\Omega_{LO} - \Delta$, see Section III.E.

together forms a dielectric capacitor. The total charge, eN_s, bound on this capacitor remains constant during the short pulses of the pumping radiation.[6] The effective charge-separation in equilibrium is denoted d and following Ref. 3 we observe that the optical excitation δn_2 *increases* this separation by

$$\delta d = \delta n_2 \times \left[\langle \Psi_2 | x | \Psi_2 \rangle - \langle \Psi_1 | x | \Psi_1 \rangle \right], \tag{31}$$

due to the finite center-of-charge separation. This increase, Eq. (31), in the effective capacitor separation is reflected in the gate-bias,

$$\frac{\Delta V_G}{V_G} = -\frac{\delta d}{d} = \frac{\left[\langle \Psi_2 | x | \Psi_2 \rangle - \langle \Psi_1 | x | \Psi_1 \rangle \right]}{d} \times \left(\frac{\delta n_2}{N_{2D}} \right). \tag{32}$$

Finally, inserting the expression for the photo-voltage , Eq. (32), into Eq. (30) finally yields an expression for the decay rate,

$$\frac{1}{\tau} = \frac{S_{FEL}(\omega)}{\omega} \sigma_{ab}(\omega) \left\{ 2 - (1 + 2n_2^0) \frac{\left[\langle \Psi_2 | x | \Psi_2 \rangle - \langle \Psi_1 | x | \Psi_1 \rangle \right] V_G}{d \Delta V_G} \right\}. \tag{33}$$

Given measurements of (a) the photo-voltage, ΔV_G, (b) the absorption cross section,* $\sigma_{ab}(\omega)$ at lasing frequency ω, and (c) the Free Electron Laser pump intensity $S_{FEL}(\omega)$, *and* a theory estimate of the center-of-charge separation,[10] Eq. (33) finally allows the experimental determination reported in Ref. 3

The set of triangles in Figure 3.6 shows, as a function of inverse temperature, these the experimentally determined net decay rates obtained at weak optical pumping, $S_{FEL} \approx 10$ mW/cm^2. We observe in particular that the weak-optical pumping decay rate remains bounded at $1/\tau \lesssim 0.03$ meV at temperatures $T < 50$ K but shows a significant temperature dependence which in Ref. 3 was fit to two thermal activation energies. For the higher-temperature regime, 25 K $\lesssim T \lesssim$ 50 K,

* Heyman *et al.* used instead an equivalent determination of the radiation transmission coefficient, see Ref. 3.

they found the thermal activation energy 24 ± 3 meV which corresponds well to the difference $\Omega_{LO} - \Delta \approx 25$ meVs between the optical-phonon frequency Ω_{LO} and the subband separation.[3] For the low-temperature regime ($T \lesssim 25$ K, however, the experimental data is fit to a thermal activation energy (~ 3 meV) of unknown origin.[3]

III.E Single-electron decay in tunneling structure

In this final section we consider the total *single*-electron decay arising with the exclusive upper-subband current injection. A central issue is whether these single-electron decay processes are faster than in the presence of a weak optical pumping of the corresponding quantum-well structure.

Formal estimates for the impurity, interface-defect, and acoustic-phonon scattering are described in Ref. 11. However, rather than providing a detailed estimate for these rates we argue below that the weak-optical-pumping experimental[3] value, $1/\tau \approx 0.03$ meV, constitute an experimental bound for the impurity, interface-defect, and acoustic-phonon scattering also with a current-injected upper-subband electron distribution (at temperatures $T \leq 50$ K.)

In contrast, we do find that the decay due to the thermally activated optical-phonon scattering, increases with the current injection. However, we still predict a vanishing rate, $\Gamma_{LO}^{ci} \leq 10^{-3}$ meV at temperatures $T \leq 25$ K. We consequently fell justified in assuming also the total *single*-electron decay rate Γ_{se} bounded by $1/\tau = 0.03$ meV at temperatures $T \leq 25$ K.

Consider first the decay due to impurity and interface-defect scattering. These intersubband decay processes are obviously elastic and are thus not effected by any Pauli exclusion even for the weakly optically pumped electron distribution. Although the current-injection may result in a wider range of possible in-plane momentum transfer, see lower left panel in Fig. I.4, the average momentum transfer is still going to be the characteristic intersubband momentum

$$q_\Delta \equiv \sqrt{2m_e^*\Delta}. \tag{34}$$

We thus expect the impurity and interface defect scattering to be almost unchanged from the weak-optical-pumping distribution and to the nonequilibrium distribution resulting from the current injection.

Consider next the decay due to the acoustic-phonon scattering. Using the formal estimates provided in Ref. 11, it follows directly (from the combined conservation of in-plane momentum and energy) that also these scattering processes are essentially elastic.* Specifically, for an electron phonon located at the bottom of the upper subband, we estimate the electron-phonon transfer at just 0.5 meV. We expect no difference between the acoustic-phonon decay rate for the weakly optically pumped distribution and the current-injected distribution arising from neither (i) the Pauli exclusion principle, of (ii) a difference in the average matrix element.

To complete our discussion of the total single-electron decay we need only consider the decay due to the optical-phonon emission. These spontaneous emission processes are of course at all experimental temperatures partially inhibited because the optical-phonon frequency $\Omega_{LO} \approx 36$ meV *exceeds* the subband separation $\Delta \approx 11$ meV. Adapting the formal treatment in Ref. 11 we have estimated

* The electron-acoustic-phonon scattering illustrated by the dashed arrow in the lower left panel of Fig. I.4 is shown with a strongly exaggerated energy transfer

the thermally activated intersubband decay rates resulting from optical-phonon-emission processes both for the optically-pumped distribution (Γ_{LO}^{op}) and for the current injected distribution (Γ_{LO}^{ci}.) The solid (dashed) curve in the *top* panel of Figure 3.6 shows our Fermi-golden-rule estimate for decay rate Γ_{LO}^{ci} (Γ_{LO}^{op}.)

In estimating the rate Γ_{LO}^{op} we have assumed that the optical pumping results in an increased upper-subband occupation density δn_2 distributed according to

$$f_2^{op}(\vec{k}) = \frac{\delta n_2}{n_1^0} \frac{1}{1 + \exp(E_{||}(k) - \mu)}, \tag{35}$$

where n_1^0 denoted the equilibrium lower-subband occupation. We have furthermore neglected all effects of the Pauli exclusion principle although there is at $T \sim 50$ K a finite occupation > 0.5 of the bottom of the lowest subband.

Although we have thus overestimated the actual decay due to the optical-phonon scattering we find a reasonable agreement between the estimated rate, Γ_{LO}^{ci} (dashed curve in top panel of Figure 3.6) and the experimentally observed[3] values of $1/\tau$. In particular, there is a reasonable agreement with the reported thermal activation energy[3]

$$E_{act} = \Omega_{LO} - \Delta \approx 24 \pm 3 \text{ meV}, \tag{36}$$

at intermediate temperatures, 25 K $\lesssim T \lesssim$ 50 K.

Consider finally the decay rate Γ_{LO}^{ci} arising from the optical-phonon emission processes with a current injected distribution. In providing this estimate we neglect again the Pauli exclusion within the lower subband and have assumeed the maximum possible upper-subband occupation given by a choice of $\phi_L = E_2$ and a complete subband occupation between E_2 and μ_L. This occupation is described by the distribution function

$$f_2^{ci}(\vec{k}) = f_{\mu_2}(E_{||}(\vec{k})) \equiv \frac{1}{1+\exp(E_{||}(k)-\mu_2)} \tag{37}$$

with *effective* upper-subband chemical potential,

$$\mu_2 \equiv \mu_L - E_2 = \mu_L - \phi_L. \tag{38}$$

The solid curve in the *bottom* panel of Figure 3.6 shows the temperature variation of this chemical potential. Nevertheless, as is clear in the *top* panel of Figure 3.6, the rate Γ_{LO}^{ci} still remains thermally activated and eventually becomes neglectable. In particular, we find that the rate can be ignored, $\Gamma_{LO}^{ci} \lesssim 10^{-3}$ meV, at temperatures $T \leq 25$ K.

In summary we have obtained an experimental bound on the total *single-*electron decay in the presence of the current injection,

$$\Gamma_{sp} \lesssim 0.03 \text{ meV}, \qquad \text{at} \quad T \leq 25 \text{ K}. \tag{39}$$

This estimate results because we can (a) assume the impurity, interface-defect, and acoustic-phonon scattering strictly bounded by the experimental value,[3] $1/\tau = 0.03$ meV, and (b) because the thermally activated optical-phonon emission can be completely ignored at temperatures $T \leq 25$ K.

Finally, we emphasize that no such experimental bound applies to the nonequilibrium electron-electron scattering even though Ref. 3 also reports measurements of the net decay rate at a strong optical pumping with a finite upper-subband occupation density $n_2 \gtrsim N_s/4$. This follows because the strong optical pumping (a) could make coherent effects very important,[7] and (b) results in a *different* nonequilibrium upper-subband occupation than with a strong current injection into the

Figure 3.1 structure. The second observation is important because the electron-electron scattering depends on the actual nonequilibrium distribution.

A detailed modeling and discussion of the intersubband decay in the presence of a strong optical pumping is beyond the scope of this dissertation. However, we *can* determine the nonequilibrium electron-electron intersubband scattering arising with the current injection into the Figure 3.1 tunneling structure and thus determine also the total intersubband decay and resulting population inversion. This motivates the study of the nonequilibrium intersubband electron-electron scattering reported on in Chapter IV.

REFERENCES

1. D. A. B. Miller, D. S. Chelma, T. C. Damen, A. C. Gossard, W. Weigmann, T. H. Wood, and C. A. Burrus, *Phys. Rev. Lett.* **53**, 2173 (1984).

2. Jerome Faist, Federico Capasso, Albert L. Hutchinson, Loren Pfeiffer, and Ken W. West, *Phys. Rev. Lett.* **71**, 3573 (1993). This paper describes and explains a corresponding voltage-drop variation of the optical selection rules.

3. J. N. Heyman, K. Unterrainer, K. Craig, B. Galdrikian, M. S. Sherwin, K. Campman, P. F. Hopkins, A. C. Gossard, To appear in *Phys. Rev. Lett.*.

4. J. N. Heyman, K. Craig, B. Galdrikian, M. S. Sherwin, K. Campman, P. F. Hopkins, S. Fafard, and A. C. Gossard, *Phys. Rev. Lett.* **72**, 2183 (1994).

5. We thank Dr. Galdrikian, UCSB for kind permission to use his Schrödinger-solver code in determining the (quasi-bound) energy levels and corresponding wavefunctions.

6. Professor James Heyman, MacAlester College; private communications.

7. Professor W. Kohn, UCSB; private communications.

8. Ned. S. Wingreen, Christopher J. Stanton, and John W. Wilkins, *Phys. Rev. Lett.* **57**, 1084 (1986).

9. A. V. Kuznetsov and C. J. Stanton, *Phys. Rev. B* **51**, 7555 (1995).

10. Dr. Bryan Galdrikian, UCSB; private communications.

11. R. Ferreira and G. Bastard, *Phys. Rev. B*, **40**, 1074 (1989).